Check for updates

FAT-GEMs: (field assisted) transparent gaseous-electroluminescence multipliers

S. Leardini[1]*, A. Saá-Hernández[1], M. Kuźniak[2], D. González-Díaz[1], C. D. R. Azevedo[3], F. Lucas[3], P. Amedo[1], A. F. V. Cortez[2], D. Fernández-Posada[1], B. Mehl[4], G. Nieradka[2], R. de Oliveira[4], V. Peskov[1], T. Sworobowicz[2] and S. Williams[4]

[1]Instituto Galego de Física de Altas Enerxías, IGFAE, Universidade de Santiago de Compostela, Santiago de Compostela, Spain, [2]Astrocent, Nicolaus Copernicus Astronomical Center of the Polish Academy of Sciences, Warsaw, Poland, [3]Institute of Nanostructures, Nanomodelling and Nanofabrication (i3N), Universidade de Aveiro, Aveiro, Portugal, [4]CERN, Esplanade des Particules 1, Meyrin, Switzerland

The idea of implementing electroluminescence-based amplification through transparent multi-hole structures (FAT-GEMs) has been entertained for some time. Arguably, for such a technology to be attractive it should perform at least at a level comparable to conventional alternatives based on wires or meshes. We present now a detailed calorimetric study carried out for 5.9 keV X-rays in xenon, for pressures ranging from 2 to 10 bar, resorting to different geometries, production and post-processing techniques. At a reference voltage 5 times above the electroluminescence threshold ($E_{EL,th}$ ~ 0.7 kV/cm/bar), the number of photoelectrons measured for the best structure was found to be just 18% below that obtained for a double-mesh with the same thickness and at the same distance. The energy resolution stayed within 10% (relative) of the double-mesh value. An innovative characteristic of the structure is that vacuum ultraviolet (VUV) transparency of the polymethyl methacrylate (PMMA) substrate was achieved, effectively, through tetraphenylbutadiene (TPB) coating of the electroluminescence channels combined with indium tin oxide (ITO) coating of the electrodes. This resulted in a × 2.25-increased optical yield (compared to the bare structure), that was found to be in good agreement with simulations if assuming a TPB wavelength-shifting-efficiency at the level of WLSE=0.74−1.28, compatible with expected values. This result, combined with the stability demonstrated for the TPB coating under electric field (over 20 h of continuous operation), shows great potential to revolutionize electroluminescence-based instrumentation.

KEYWORDS

MPGD (micropattern gaseous detector), electroluminescence (EL), GEM (gas electron multiplier), rare event searches, TPC (time projection chamber)

1 Introduction

The term electroluminescence (EL) is often used, among others, to refer to the detection principle introduced by Conde and Policarpo in the 60s (Alves and Policarpio, 1967; Conde and Policarpo, 1967; Conde et al., 1968). In its simplest description, within this context, it might be seen as the mechanism by which to enhance the ionization response of a gaseous detector, converting ionization electrons (difficult to count) into photons (easy to count) by means of an electric field. Since the accelerated swarm of electrons experiences different energy thresholds for excitation and ionization, the net result is the appearance of an electric field regime where it is possible to have the former without the latter. In noble gases, specifically, the high VUV-scintillation probability per excited state (Serra et al., 2015; Azevedo et al., 2018) results in strong scintillation yields (Y) of up to easily 1,000s of ph/e, yet in the absence of avalanche multiplication (Monteiro et al., 2008; Freitas et al., 2010). These are the conditions under which EL exhibits its most remarkable features and finds widespread use: in the avalanche-free regime, as noble gases possess no inelastic degrees of freedom other than excitations, nearly all energy gained by electrons in the electric field (qV) turns into scintillation photons, leading to an approximately linear response (Oliveira et al., 2011). This can be expressed handily as:

$$Y \simeq K(V - V_{th}) \qquad (1)$$

$$Y_z/N \simeq K(E^* - E_{th}^*). \qquad (2)$$

The second expression conveys the fact that, when the density-reduced electric field ($E^* = E/N$, a measure of the characteristic electron energy) is above a threshold value needed to excite the medium (E_{th}^*), any additional energy gained in the field goes into new excitations. In the above equations K is a proportionality constant, Y refers to the scintillation yield, Y_z to the yield per unit length and N is the number of atoms per unit volume. The high efficiency of the EL process has a second consequence, that represents perhaps one of its best known properties: the relative variance of the electroluminescence signal ($Q = (\sigma_Y/Y)^2$) is very small. Its contribution to the calorimetric response of a gaseous detector propagates into the energy resolution (FWHM) as:

$$\mathcal{R} = 2.355 \sqrt{F + Q + \frac{1}{n_{pe}}\left(1 + \frac{\sigma_G^2}{G^2}\right)} \sqrt{\frac{1}{n_e}}. \qquad (3)$$

In the above expression F represents the Fano factor of the medium (0.1–0.2 in noble gases (Aprile et al., 2006)), n_{pe} is the number of detected photons ('photoelectrons') per electron, and σ_G/G refers to the relative width of the single-photon distribution function of the photosensor. The last term involves the number of ionization electrons, $n_e = \varepsilon/W_I$, with ε being the energy deposited in the medium and W_I the average energy needed to release an electron (Blum et al., 2008). The term Q is generally so small (Escada et al., 2011; Oliveira et al., 2011) that it has eluded experimental determination except in the presence of electronegative gases such as CO_2 (Henriques et al., 2017). Due to the smallness of Q, as soon as the number of detected photons per primary electron is of the order of $n_{pe} = 10$ or more, the energy resolution will approach the intrinsic limit of the gas medium (Nygren, 2009).

The aforementioned characteristics make electroluminescence, nowadays, the workhorse of many experiments based on Time Projection Chambers (TPCs) in the field of Rare Event Searches (Irastorza et al., 2013), such as XENON (Aprile et al., 2023), LZ (Aalbers et al., 2023), PandaX (PandaX Collaboration, 2023), and DarkSide (Aalseth et al., 2020) (aimed at direct WIMP Dark Matter detection) or NEXT (Novella et al., 2022) (aimed at measuring $\beta\beta0\nu$ decay). Its use is foreseen in upcoming experiments such as RED (Akimov et al., 2022) and GANESS (Monrabal, 2021) (aimed at precision studies of coherent neutrino scattering), and it can be found, too, in applied research for instance in proposals for Compton cameras (Azevedo et al., 2013) and Compton dispersion at next-generation Light Sources (Saá-Hernández et al., 2021). In such experiments, the single-electron detection capabilities of electroluminescence are essential to extend WIMP sensitivity down to very low masses (e.g., (Agnes et al., 2023)), while near-Fano energy resolution is required for precise calorimetry in $\beta\beta0\nu$ searches, thus avoiding contamination from $\beta\beta2\nu$ decays and natural radioactivity (Novella et al., 2023). High-rate environments like (Azevedo et al., 2013; Saá-Hernández et al., 2021) benefit from the absence of ion feedback and subsequent high rate capability stemming from the avalanche-free nature of the electroluminescence process.

For all their beauty, the electroluminescence process in presently running experiments is invariably implemented based on early designs relying on wires or meshes, and suffer from the inevitable scaling-up limitations due to electrostatic sagging and deformation (Rogers et al., 2018) and, chiefly, defects (Discussions at the Conference, 2023). During the operation of the NEXT-NEW detector, for instance, the pressure-reduced electric field was 1.2 kV/cm/bar at 10 bar, a mere 0.5 kV/cm/bar above the EL threshold and 3 times below the values achieved in the present work and, generally, on small R&D setups. Thus, when possible, the commissioning of the EL-region becomes a separate endeavour, requiring purposely-built chambers several square meter in size, essentially as large as the final operating conditions demand (Müller, 2022). Given that experiments keep increasing in size to achieve sensitivity, it seems very unlikely that the situation will improve except if new production techniques are introduced.

Lately, over the last 5–10 years, there has been interesting progress on the development of optically-enhanced structures, and we follow this lead. Transparent substrates like glass, for instance, have been successfully carved into gaseous electron multipliers (GEMs), be it by photolitography (Takahashi et al., 2013) or sand-blasting (Lowe et al., 2021). They are sturdy and immune to sagging or deformation, and can be easily tiled to cover large areas (Lowe et al., 2023). At the thicknesses and hole sizes needed for efficient electroluminescence (several mm), structures based on the highly VUV-reflective Teflon (Ban et al., 2017) or relying on the transparency of PMMA (González-Díaz et al., 2020) have been manufactured by CNC drilling. In order to achieve VUV-transparency, the solid wavelength-shifter polyethylene naphthalene (PEN) was proposed as a bulk material and successfully machined and operated under Xe and Ar for the first time in (Kuźniak et al., 2021). A natural continuation of the previous works was to resort to TPB coating of the (PMMA-based) GEM channels, theoretically enabling higher wavelength-shifting yields compared to PEN plates. Aiming at wide range of applications, in particular those related to

TABLE 1 Compilation of the FAT-GEM structures characterized in this work.

Descriptor	Hole size (mm)	Pitch (mm)	Thickness (mm)	Number of holes	TPB	ESR
A	1	5	4.5	30	No	No
B	2	5	4.7	30	No	No
C	3	5	4.75	30	No	No
D	4	6	4.8	18	No	No
E	2	5	5.33	31	Yes	No
F	2	5	5.47	31	Yes	Yes

Rare Event Searches, the core materials of such EL-structures are chosen to be radiopure.

Here we present a comprehensive performance study of different FAT-GEM structures under 5.9 keV X-rays, involving different fabrication procedures, different processing (adding wavelength-shifting coating or an internal reflective layer), different geometries (hole sizes), different gases (xenon and argon), and different pressures (2–10 bar). Comparisons with simulations and with a simple 2-mesh configuration are given too.

2 FAT-GEMs

2.1 Fabrication process

Results from micropattern gas detectors (MPGDs) operated in avalanche mode in gaps as small as 50 μm (typical GEM thickness) suggest that they can potentially produce a high optical output in a noble gas (Monteiro et al., 2012). Electroluminescence, on the other hand, benefits from electrified regions where the product of the number density, N, times gas gap, d, is much larger (up to $P \cdot d \sim$ 10 bar·cm at room temperature, compared to $P \cdot d \sim 5 \times 10^{-3}$ bar·cm for GEMs at around atmospheric pressure). Geometries with larger values of the product $N \cdot d$ can sustain higher breakdown voltages (Norman et al., 2022) and therefore provide higher optical gains in avalanche-free conditions (Eq. 2). In regard to the electric field configuration, an uniform field region is preferable in terms of intrinsic energy resolution (Escada et al., 2011) and maximum optical throughput before the onset of multiplication (e.g., (Freitas et al., 2010; Leardini et al., 2022)). Coincidentally, a high $N \cdot d$ enhances neutral bremsstrahlung radiation below the E_{EL} threshold, too (Henriques et al., 2022; Bondar et al., 2023). The main objection against employing large EL gaps is the presence of sagging and deformation when such uniform fields are created by means of meshes or wires suspended on m² areas and beyond (Escada et al., 2011; Rogers et al., 2018).

Thus, in order to create a large-gap, uniform-field, sagging-free structure, PMMA plates of about 5 mm-thickness were procured, drilled at different hole diameters (1–4 mm) on an hexagonal pattern, with a pitch of 5–6 mm. Two additional structures were prepared based on the 2 mm-hole geometry, this time having TPB coated inside the holes. One of them had an additional 3M™ Enhanced Specular Reflector (ESR) layer (Weber et al., 2000; Application Guidelines ESR Family, 2018) placed underneath the cathode. A compilation of the structures studied is provided in Table 1.

Regular (uncoated) structures were produced in the RD51 workshop at CERN: a bare PMMA plate (7 cm × 7 cm) was thermally bonded to two circular copper electrodes (6 cm diameter).[1] Holes were then CNC-drilled, and a rim around them (0.2 mm) was created in a chemical bath, to mitigate corona discharges. Finally, a hatched pattern (inner square side 0.35 mm, trace width 0.1 mm) was made through photolithography on the cathode of the structure. Two things were noticed: on the positive side, electric field simulations showed a negligible change in the electric field compared to the geometry with a solid cathode; on the negative side, thermal-bonding rendered the structure translucent and sub-optimal for further optical treatment, something that was pursued through an alternative fabrication process that is discussed below. Two microscope photos of the resulting structures are provided in Figures 1A, B and the fabrication procedures are sketched in Figure 1C.

The TPB-coated structures were produced at AstroCeNT (Poland), starting from the application of thin PET films coated with ITO to the two faces of the bare tile, by means of an adhesive film. Compared to the thermally-bonded hatched electrode (transparency 60%), the PET+ITO resulted in a larger transparency of 79% (according to the producer (Visiontek Systems Ltd., 2023)), with the benefit of preserving the optical properties of the plate. Once the PET-ITO films were adhered, holes were made with a manual milling machine equipped with precision drill bits, and finally TPB evaporated inside them (Figure 1D). In order to further increase light collection, an ESR layer was interleaved in between the PMMA and the ITO electrode for one of the structures (Figure 1E). The thickness of the plates was around 4.7 mm for the uncoated structure and 5.4 mm for the coated ones.

2.2 Radiopurity

A mid-size FAT-GEM of 18 cm diameter was purposely-built at the CERN-RD51 workshop and screened mainly to show that the production process did not result in strong contamination. The raw PMMA material was Polycast provided by Spartech (as used in the DEAP-3600 detector), with measured activities as low as

---

1 The metallization area was increased with respect to the structures used earlier in (González-Díaz et al., 2020), leaving the active area unchanged, to eliminate possible fringe-fields stemming from charging-up.
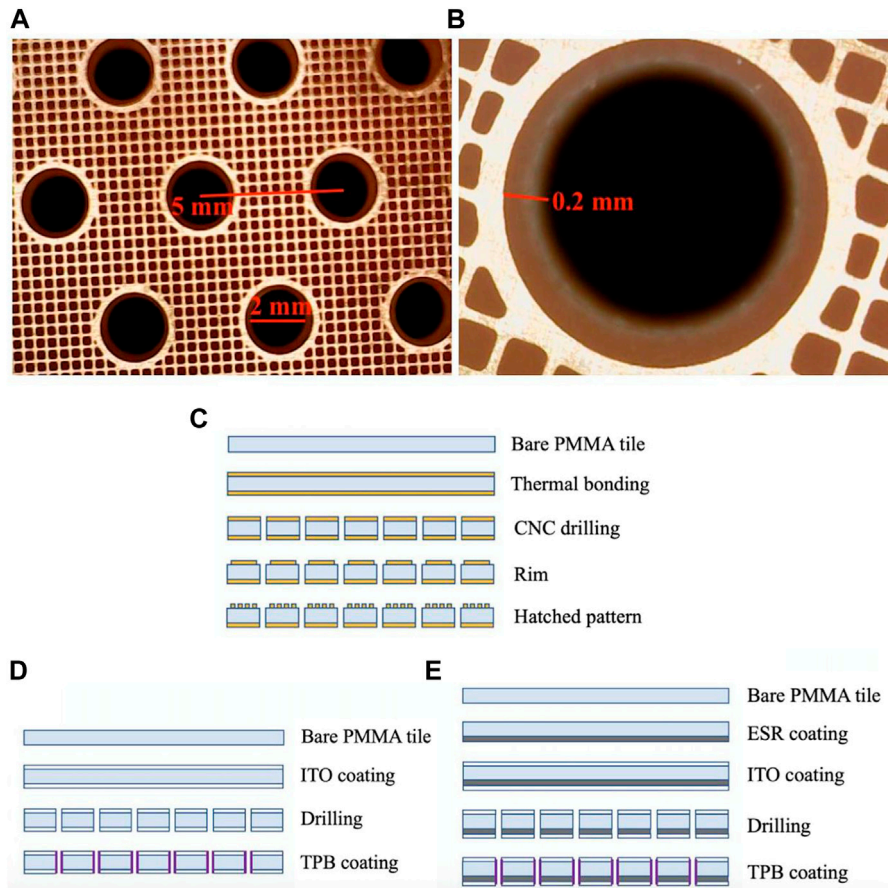
FIGURE 1
(A, B) uncoated FAT-GEM "B" (the hatched-electrode technique was employed in this particular case). **(C−E)** Sketch of the fabrication process for FAT-GEMs produced at CERN **(C)** and at AstroCeNT **(D, E)**. FAT-GEMs produced at CERN have thermal-bonded copper electrodes, one of them made semi-transparent through chemical etching of a hatched pattern. For the structures produced at AstroCeNT, ITO electrodes were applied in order to increase the structure transparency; moreover, TPB was coated inside the holes. Procedures **(D, E)** differ for the presence of a reflecting ESR layer.

FIGURE 2
Bare PMMA plate (left) and FAT-GEM (right) inside the copper shielding of the setups used for radioactivity screening at Laboratorio Subterráneo de Canfranc.

TABLE 2 Measurements of radiopurity performed at the Canfranc Underground Laboratory for the bare PMMA (second column) and for a FAT-GEM with thermally-bonded copper electrodes (third column). The last column shows the measurements of the PMMA light guide from the DEAP-3600 detector (Amaudruz et al., 2019). Only upper limits are reported, driven by the sensitivities of the respective assays.
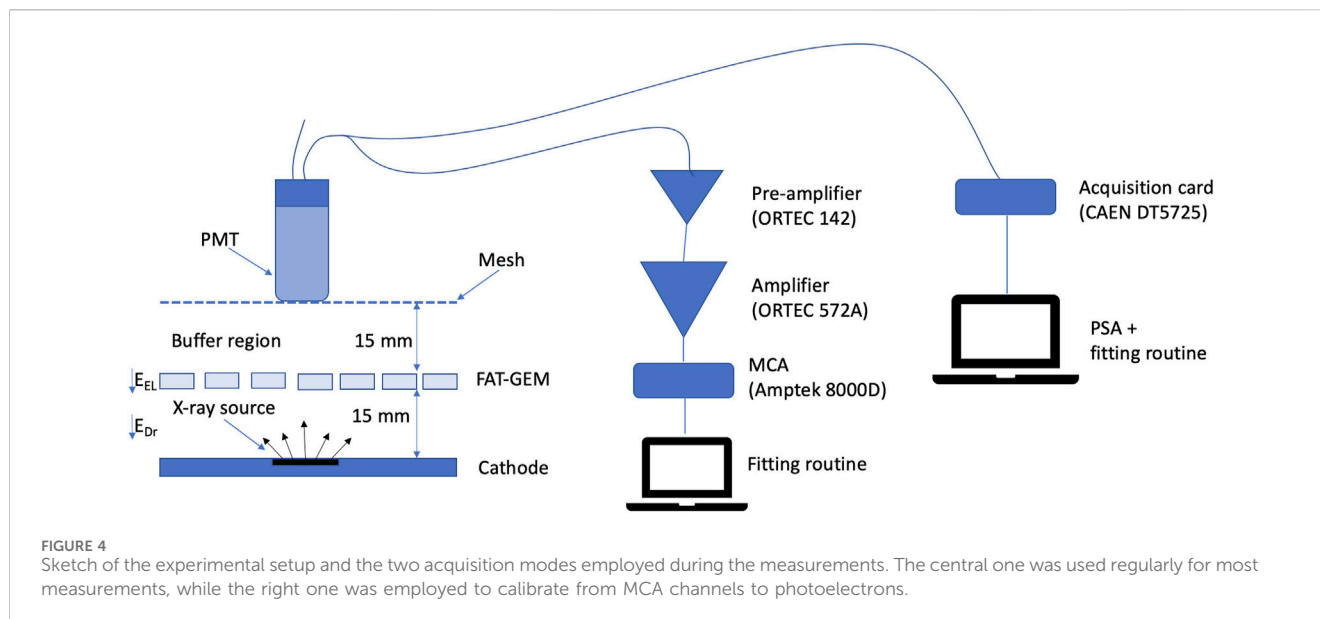
Isotope	PMMA (mBq/kg)	FAT-GEM (mBq/kg) [(mBq/cm^2)]	PMMA, DEAP-3600 (mBq/kg)
U-238/Pa-234m	< 340	< 791 [< 0.741]	
U-238/Pb-214	< 2.8	< 6.9 [< 0.006]	
U-238/Bi-214	< 2.3	< 7.0 [< 0.007]	
U-238/Ra-226			< 0.1
U-238/Th-234			< 9.0
Th-232/Ac-228	< 8.8	< 22 [< 0.021]	
Th-232/Pb-212	< 2.9	< 7.4 [< 0.007]	
Th-232/Tl-208	< 6.3	< 15 [< 0.014]	
Th-232			< 0.3
U-235/U-235	< 1.9	< 6.1 [< 0.006]	< 0.6
K-40	< 17	< 38 [< 0.036]	< 1.1
Co-60	< 0.74	< 2.5 [< 0.002]	
Cs-137	< 1.1	< 1.9 [< 0.002]	

FIGURE 3
Illustration of the FAT-GEM concept. The electron enters from above into the channels due to the intense electric field, and produces electroluminescence (VUV). The light is subsequently wavelength-shifted into the visible range through TPB-coating of the holes' walls, reflected at the cathode inner surface and transmitted through the transparent anode until it reaches the photosensor.

0.11 mBq/kg of [235]U (Amaudruz et al., 2019). The radiopurity screening was performed at Laboratorio Subterráneo de Canfranc over a practical time of a bit over a month (50.76 days at GeAnayet for the bare PMMA plate, 47.7 days at GeTobazo for the FAT-GEM, Figure 2). The sensitivity of the measurements, presented in Table 2, was mainly limited by the mass of the amplification structure. While competitive radiopurity levels would still need to be demonstrated (especially for a structure that is expected to face the interaction volume), in the light of our current measurements the present fabrication techniques seem promising.

2.3 Working principle

Having a cutoff typically in the range of 300 nm (Tameda et al., 2019), PMMA is not a VUV-transparent material. Therefore, without further treatment, it is not optimal for use under noble gas scintillation as the amount of light detected would be limited by the solid angle defined by the holes' walls. In principle, coating the walls with TPB should allow to make use of such a 'lost' light at near 100% efficiency (Kuźniak and Szelc, 2020), re-emitting it isotropically in a band (peaked at λ ~420 nm, with a cutoff

FIGURE 4
Sketch of the experimental setup and the two acquisition modes employed during the measurements. The central one was used regularly for most measurements, while the right one was employed to calibrate from MCA channels to photoelectrons.

around $\lambda \sim 350$ nm (Benson et al., 2018)) to which the PMMA is fully transparent. Additionally, a reflective layer would help recovering part of the wavelength-shifted light that is emitted in the opposite direction with respect to the light sensor (Figure 3).

3 Experimental methods

3.1 Setup

The setup used was the same as in previous works (González-Díaz et al., 2020; Kuźniak et al., 2021): the electroluminescent structures served as the anode of a drift/conversion region of 15 mm in length, closed by an aluminum cathode with an x-ray source (^{55}Fe) placed behind it (Figure 4). Initially, a high-transparency mesh was placed covering the anode of the amplification structures, but it was removed once assessed, comparing the yield curve of the same structure with and without it, that it had a negligible impact on the performance. At 15 mm from the FAT-GEM anode, a Hamamatsu R7378 PMT was placed, covered with a grounded mesh to eliminate fringe-fields from the buffer region leaking into the PMT vacuum. The PMT was then connected to a pre-amplifier (ORTEC 142), an amplifier (ORTEC 572A) and finally to an MCA (Amptek 8000D) to collect the spectra. In order to convert from MCA channels to photoelectrons, a calibration run was performed by connecting the PMT directly to an acquisition card (CAEN DT5725), as described later.

A sketch of the experimental setup and a description of the acquisition system can be seen in Figure 4. The container vessel was connected to a pressure/vacuum system and, before filling, it was pumped down to 10^{-4} mbar. During operation the gas was circulated through a cold getter (Entegris GPU80) specified to trap H_2O and O_2, with a KNF compressor (N286.15) at around 20 Nl/min.[2]

During the argon measurements, high-purity fresh gas (6N bottle, i.e., ppm-level contamination) was used for each run (namely, for each EL-field series). During the measurements with xenon, on the other hand, the gas was cryorecovered after each run and residual impurities were pumped away. Variations in the yields were observed during the measurements and estimated to typically represent a 15%. They were attributed to gas contamination and PMT drifts.

3.2 Data taking and analysis

For each structure, the electroluminescence field (E_{EL}) was kept fixed while scanning the drift field (E_{Dr}), to achieve the highest electron transmission (a detailed explanation is provided in Section 5.1). With the drift field fixed at that value, a scan for different electroluminescence field values was performed. MCA spectra were then stored, rebinned, background-subtracted and finally fitted to a gaussian (Figure 5). Apart from the electronic noise at low channel count, there was a second source of background on the left hand-side of the spectra correlated with activity in the buffer region (between the structure and the PMT-mesh) when the anode of the FAT-GEM was positively biased (Figures 5A). Although the size of the buffer region was chosen such that the electric field there was above the electroluminescence threshold at all times (maximum value of 533 V/cm/bar), the background was seen to increase with pressure, pointing to the presence of a scintillation mechanism different from electroluminescence. The only available phenomenon outside corona effect stemming from the connection points (not expected as those were smoothed and screened with black tape), is the direct radiative emission of the drifting electrons in the form of neutral/dipolar bremsstrahlung (Henriques et al., 2022). This source of background was assessed by a dedicated run with the 2 mm-hole structure, taking spectra at the same drift and electroluminescence fields, but with the anode of the structure grounded (Figures 5B). Figure 5C shows for reference a
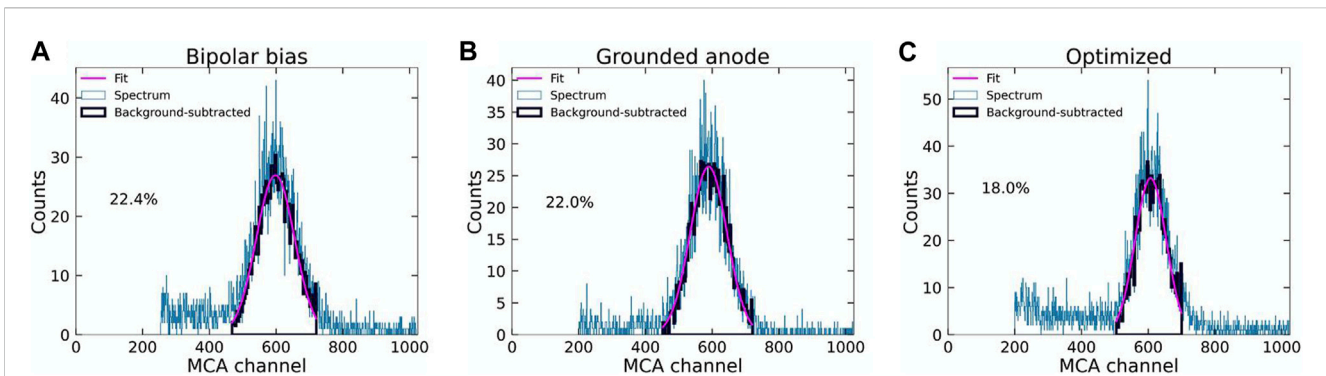
---

2   Normal liters per minute.

FIGURE 5
(A, B): exemplary spectra taken with the MCA (2 mm structure, p=2 bar, E_{Dr}=167 V/cm/bar, E_{EL} = 4.6 kV/cm/bar), with a Gaussian fit superimposed (22.4% FWHM -A), and 22.0% FWHM -B), respectively). This run corresponds to a control measurement performed with bipolar bias (A) and grounded anode (B). The difference in background activity is attributed to the buffer region and was subtracted during analysis. (C): MCA spectrum taken for the 2 mm structure at p=2 bar, E_{Dr}=167 V/cm/bar, E_{EL} = 6.9 kV/cm/bar, corresponding to an energy resolution of 18% FWHM. The PMT voltage was lower for this point than for the spectra in (A, B), in order to match the MCA range.

spectra taken close to the optimal electric field (maximum transmission and highest electroluminescence field). At the highest pressures, when bipolar biasing of the FAT-GEMs was unavoidable due to power supply limitations, the background subtraction was implemented to extract the energy resolution.[3]

In order to convert from MCA channels to photoelectrons, a two-step procedure was followed: first, the PMT was calibrated according to the procedure described in (Leardini et al., 2022): a green LED was powered with a fast pulser (Agilent 81130A), adjusting the bias voltage until it resulted in a light intensity around the single-photon level. Data was then taken with an acquisition card (CAEN DT5725) and fitted with gaussians, whose integral values were bound by Poisson statistics. Second, a dedicated run with the 2-mm uncoated structure was performed, setting the same values of drift and electroluminescence fields as for the data taken with the MCA. Through a pulse-shape analysis and fitting routine, and resorting to the single-photon calibration, the number of photoelectrons/electron was obtained. Finally, the slope between the number of photoelectrons/electron and the peak position in the MCA data was found by performing a linear fit, providing the calibration value (Figure 6, left).

Since different PMT biases were used during the measurements, the relation between gain and voltage was assessed with an LED. The

data was then fitted to a power-law, showing agreement with the data-sheet from the manufacturer (Figure 6, right).
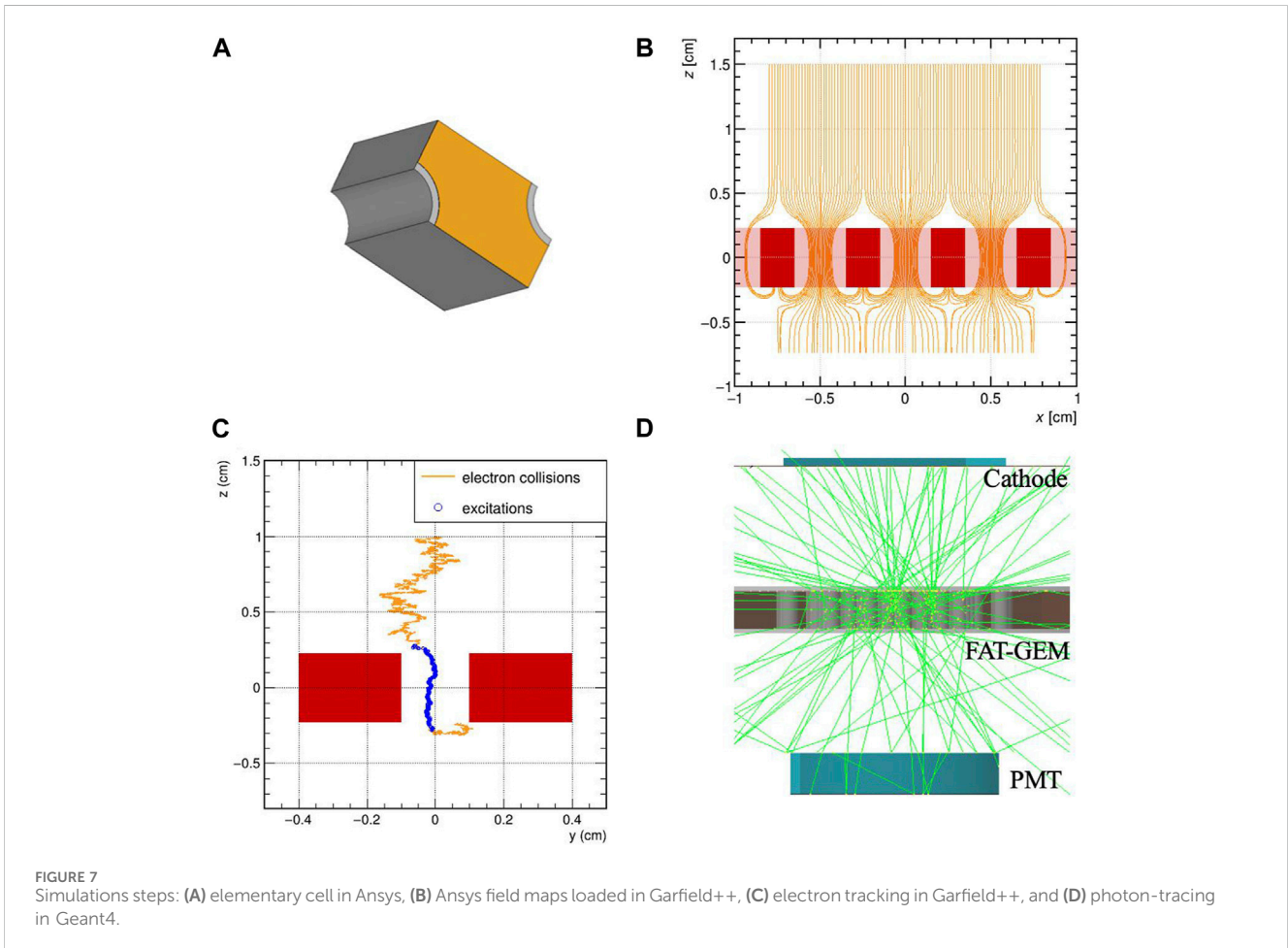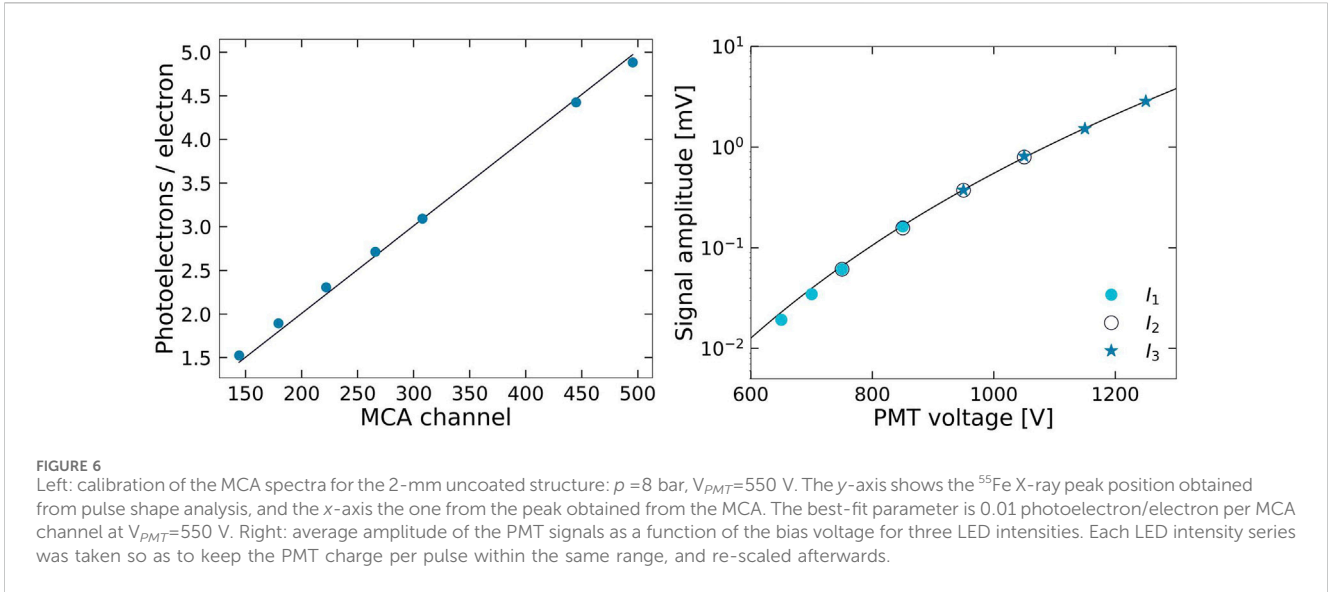
4 Simulations

Simulations were performed according to the following steps. First, the electric field maps ensuing from an elementary amplification cell were created with Ansys (ANSYS, 2023), (Figure 7A). Field and geometry maps were then imported into Garfield++ (Schindler, 2019) and extended in the x and y axis (axes parallel to the electrode plane), building the FAT-GEM structure (Figure 7B). The position of the primary electrons was generated following an uniform x, y distribution centered at the middle of the detector, extending over a ±5 mm region and placed at 0.1 mm from the cathode plane. The impact of considering a distributed ionization source corresponding to the X-ray mean free path (around 2.7 mm/bar) was evaluated but the differences dimmed too small. In Figure 7C the path of an electron is shown: as expected, most of the collisions that produce an excited state happen inside the FAT-GEM hole.

The Garfield++ simulation provided the 3D-distribution of excited states over the entire array of holes. This was then imported into Geant4 (Agostinelli et al., 2003) and used to sample the initial positions of the scintillation photons, that were subsequently launched isotropically.[4] Photon ray-tracing was handled by a Geant4 model with optical properties implemented for all materials, extending the model used in Ref. (Kuźniak et al., 2021). New wavelength-dependent optical properties added to the model included the transparency of ITO (approx. 79%, based on the suppliers' specification (Visiontek Systems Ltd., 2023)), measured reflectivity for the laminated ESR foil, and TPB properties as in (Boulay et al., 2021). This allowed us to estimate the geometrical

---

3   The analysis procedure is as follows: i) an iterative gaussian fit was performed, over a running window defined from the width of the [55]Fe energy distribution; ii) once the algorithm converged to the estimates of the peak position and width, the background was defined as any entry outside a ±2.5σ band around the peak position; iii) the background was then fitted to a straight line and the interpolated value subtracted from the energy distribution; iv) the gaussian fit was repeated, providing the final values. Studies performed in equivalent conditions, with and without background, allowed to assign the uncertainty of the procedure to be about 1% (relative), that is included in the uncertainty of the energy-resolution data.

4   A control simulation considering excited states produced only in the central hole yielded little differences.

FIGURE 6
Left: calibration of the MCA spectra for the 2-mm uncoated structure: p =8 bar, V_{PMT}=550 V. The y-axis shows the ^{55}Fe X-ray peak position obtained from pulse shape analysis, and the x-axis the one from the peak obtained from the MCA. The best-fit parameter is 0.01 photoelectron/electron per MCA channel at V_{PMT}=550 V. Right: average amplitude of the PMT signals as a function of the bias voltage for three LED intensities. Each LED intensity series was taken so as to keep the PMT charge per pulse within the same range, and re-scaled afterwards.

FIGURE 7
Simulations steps: **(A)** elementary cell in Ansys, **(B)** Ansys field maps loaded in Garfield++, **(C)** electron tracking in Garfield++, and **(D)** photon-tracing in Geant4.

efficiency of the experimental setup (Figure 7D). A two-mesh configuration was simulated using similar techniques, except that the mesh transparency was introduced as an effective number and the reflectivity of the aluminum cathode (Lindseth et al., 1999) was

included too (yielding about a 10% increase, an effect negligible for FAT-GEMs).

Finally, photon detection efficiency (PDE) curves were considered for four illustrative sensors: Hamamatsu R7378
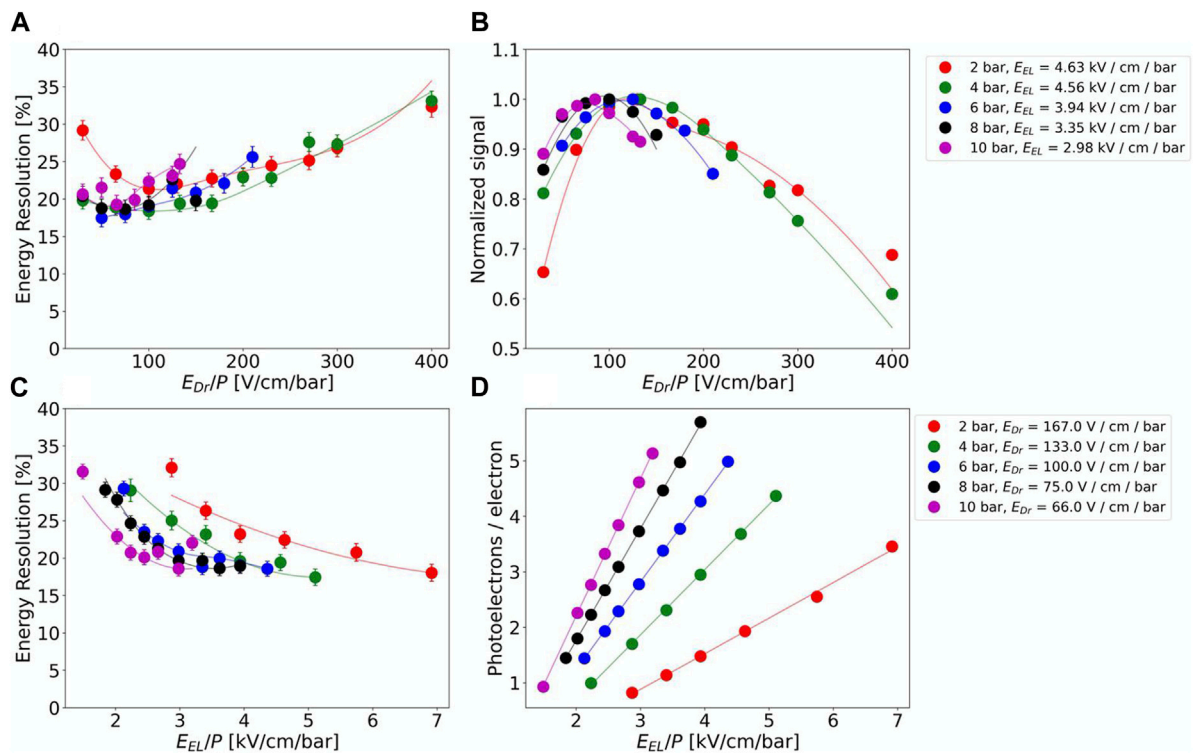
FIGURE 8
Drift field **(A, B)** and EL field **(C, D)** scans for the uncoated 2 mm-hole FAT-GEM. The lines for the energy resolution and the transmission curves are splines meant to guide the eye.

(hamamatsu.com, 2024) (employed in these measurements), R11410-21 (used in XENON1T (PhotoMultiplier tubes and assemblies, 2024)) PMTs, and two representative SiPMs: FBK NUV-HD-SF (Aalseth et al., 2018) and Hamamatsu VUV4 (S13370) (Gallina et al., 2019).

5 Results

5.1 Untreated FAT-GEMs

In Figure 8, the characterization of the uncoated 2 mm-structure is reported. Data were taken with xenon gas at 2, 4, 6, 8, and 10 bar. The plots labeled as a and b refer to the drift-scan measurements: on the left the energy resolution (FWHM), on the right the light yield normalized to the maximum ('transmission' curve). The decrease of transmission at high drift fields can be explained by the loss of field-focusing: the electron, under a strong drift field, hits the surface of the structure instead of being channeled into the holes. The decrease of transmission at low fields is qualitatively reproduced by simulations too (Figure 9) and can be attributed partly to electroluminescence extending outside of the hole region and increasing as the drift field increases. However the much stronger trend in data suggests the presence of additional contributions (presumably due to attachment to impurities).
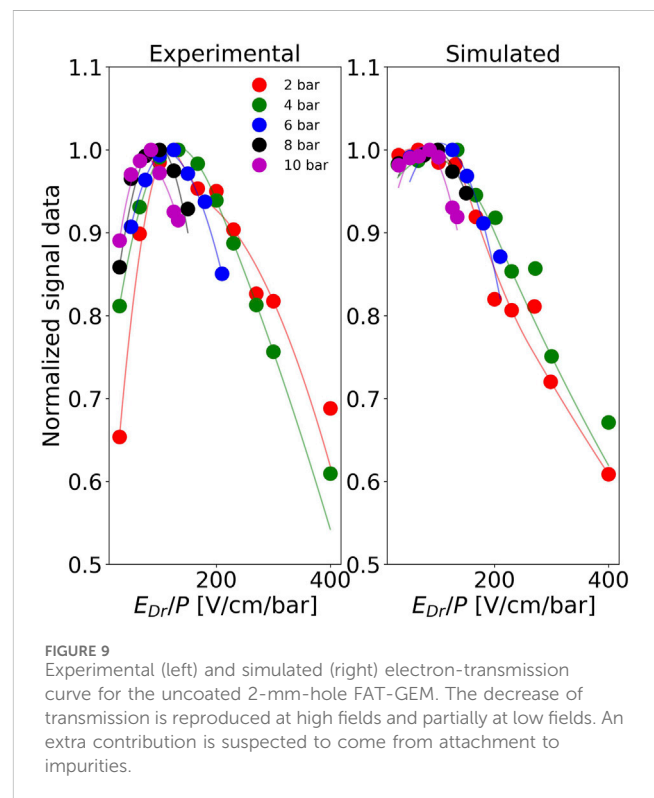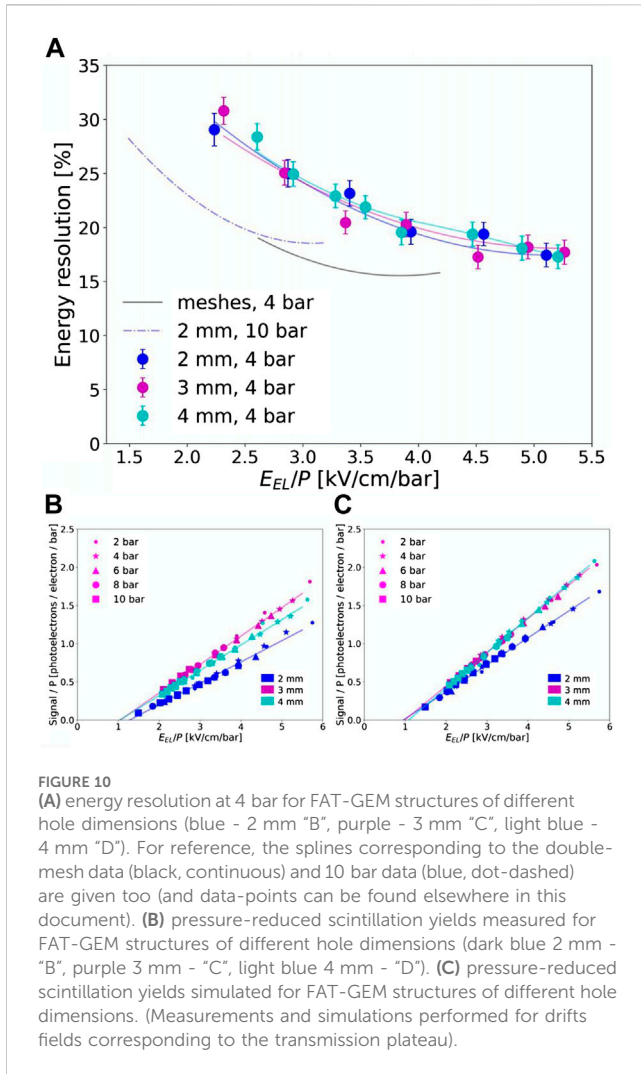

FIGURE 9
Experimental (left) and simulated (right) electron-transmission curve for the uncoated 2-mm-hole FAT-GEM. The decrease of transmission is reproduced at high fields and partially at low fields. An extra contribution is suspected to come from attachment to impurities.

FIGURE 10
(A) energy resolution at 4 bar for FAT-GEM structures of different hole dimensions (blue - 2 mm "B", purple - 3 mm "C", light blue - 4 mm "D"). For reference, the splines corresponding to the double-mesh data (black, continuous) and 10 bar data (blue, dot-dashed) are given too (and data-points can be found elsewhere in this document). **(B)** pressure-reduced scintillation yields measured for FAT-GEM structures of different hole dimensions (dark blue 2 mm - "B", purple 3 mm - "C", light blue 4 mm - "D"). **(C)** pressure-reduced scintillation yields simulated for FAT-GEM structures of different hole dimensions. (Measurements and simulations performed for drifts fields corresponding to the transmission plateau).

Figures 8C, D shows the results of the electroluminescence scan: on the left the energy resolution, on the right the detected number of photons/electron, namely, photoelectrons/electron (n_{pe}). One can see that the scintillation yield increases with pressure as expected, except for 10 bar where the voltage limit of our power supplies is reached. The voltage drop across the FAT-GEM amounts to 15 kV in those conditions.

The 'typical' best energy resolution was 17%–17.5%, obtained for virtually any structure and pressure, at high E_{EL} fields (Figure 10A). A dedicated run with xenon at 4 bar and meshes (electroluminescence gap of 5 mm) yielded an energy resolution a bit over 15% despite the much increased scintillation (the mesh results are shown through the continuous line in Figure 10A).

In Figure 10B the pressure-reduced yields are shown for the three uncoated structures and all pressures. All points fall on a line, showing that operation takes place in pure EL-mode, i.e., largely free from avalanche multiplication. Comparing the results with simulations (Figure 10C), the latter predict slightly larger yields: 15% (2 mm), 22% (3 mm), 30% (4 mm). Remarkably, both in simulation and measurements, the threshold to have scintillation light is observed to be 1 kV/cm/bar (above the canonical 0.7 kV/cm/

bar for uniform-field conditions in xenon (Henriques et al., 2022)) for all structures. The increase can be interpreted as the lower effective field in the central axis of the hole (where electrons are field-focused) compared to a parallel-electrode configuration. In data, a small deviation is observed for 2 mm structures, providing a hint that the yields at high E_{EL}/P and low P might have a small contribution from avalanche multiplication, biasing the linear fit towards higher threshold values.

An additional structure with 1 mm hole size was characterized, yielding a factor × 3 less light than the 2 mm structure. This seems to support the expectation from simulation, where a minimum diameter size of 1.75 mm is needed in order to reach 100% 'entrance × transmission' probability for the impinging electron, on a 5 mm-long xenon channel at typical EL fields.

5.2 TPB-coated FAT-GEMs

A direct assessment of the impact of TPB at the holes' walls was made for the 2 mm structure under argon, since our PMT has a fused-silica window and is therefore blind to its scintillation. As expected, no signal was observed before coating with TPB, however a clear spectrum was formed after doing so (Figure 11, dark-blue circles).
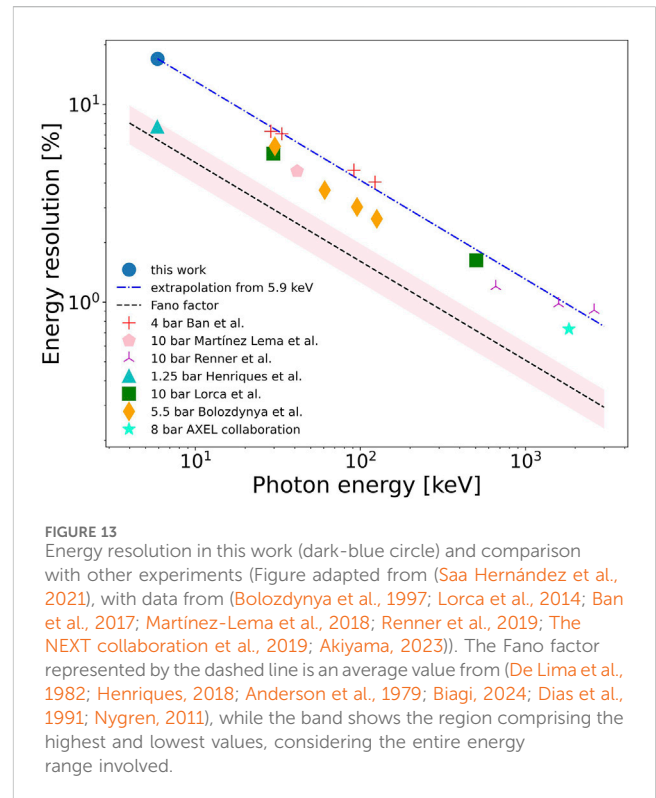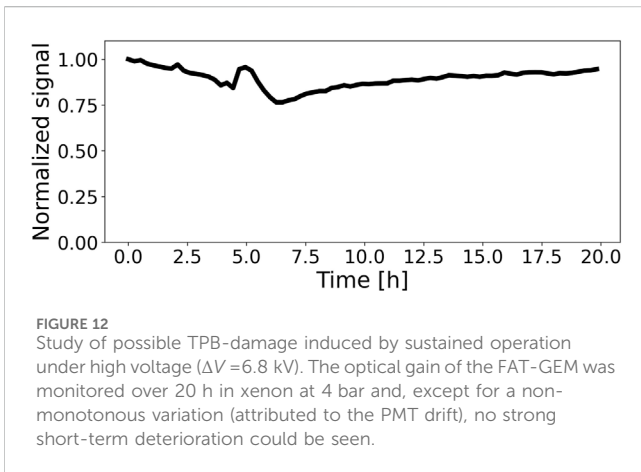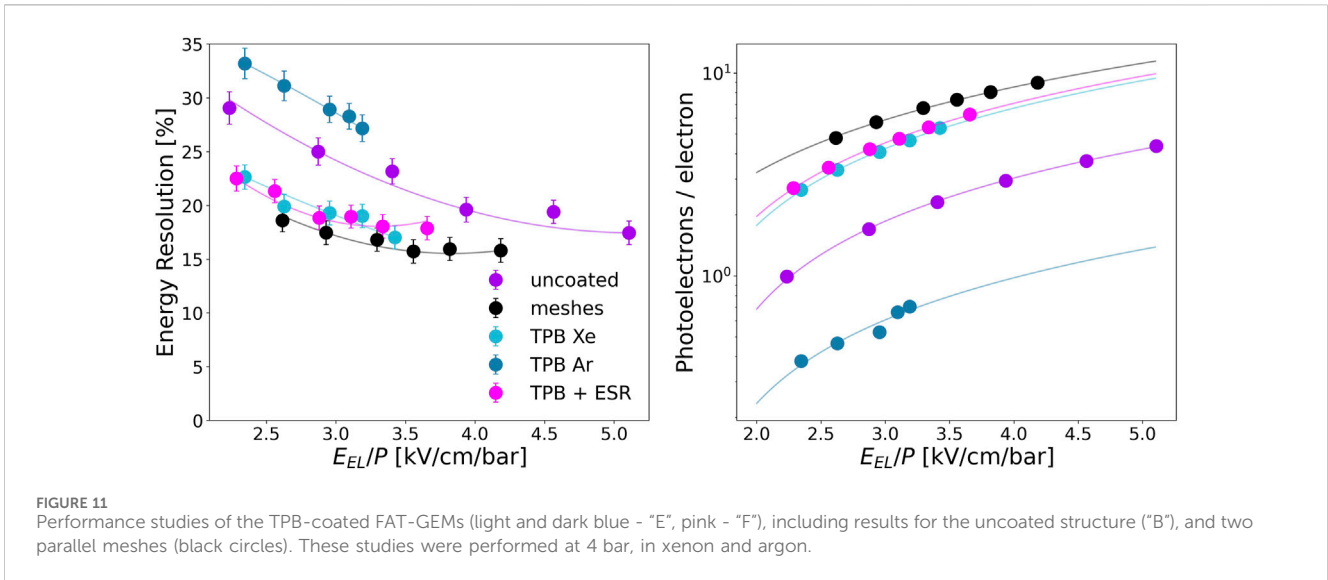
A run with xenon at 4 bar showed a 125% average increase of detected light with respect to the uncoated structure, resulting on a mere 25% deficit with respect to meshes at the maximum operating field of 3.5 kV/cm/bar (Figure 11, light-blue circles). Such a field was significantly lower than the 5 kV/cm/bar applied to the uncoated structures and was chosen simply to fully preserve the structure for further studies, avoiding risk of discharges and TPB damage. At that field, the energy resolution was comparable with the one provided by the two-mesh setup (Figure 11, left).

A structure with ESR was also tested in xenon at 4 bar (pink circles), providing just 6% more light than the coated structure without reflector. As discussed later in text, such a modest increase can be understood largely due to the presence of internal reflection inside the PMMA, due to the specular-reflection characteristics of ESR, and/or a bad optical coupling. A path to improve this performance is discussed later in text.

Short-term aging of the TPB-coated FAT-GEMs was studied in xenon at 4 bar, operating the structure with ΔV=6.8 kV continuously over 20 h (event rate ~5 Hz). Non-monotonous variations within a maximum of 25% were observed, attributed mainly to PMT drifts. The strong correlation with the temperature variation during a day-night cycle suggests that this transient behaviour arises from small variations in the electrical properties of the passive components of the base (Figure 12). No indication of permanent damage was evident after the test.

6 Discussion

The best energy resolution that was measured for FAT-GEMs in this work was 17% (FWHM), at the 5.9 keV peak of ⁵⁵Fe. This represents almost a factor two increase with respect to the value expected from the Fano factor alone (De Lima et al., 1982; Henriques, 2018; Anderson et al., 1979; Biagi, 2024; Dias et al.,

FIGURE 11
Performance studies of the TPB-coated FAT-GEMs (light and dark blue - "E", pink - "F"), including results for the uncoated structure ("B"), and two parallel meshes (black circles). These studies were performed at 4 bar, in xenon and argon.

FIGURE 12
Study of possible TPB-damage induced by sustained operation under high voltage (ΔV =6.8 kV). The optical gain of the FAT-GEM was monitored over 20 h in xenon at 4 bar and, except for a non-monotonous variation (attributed to the PMT drift), no strong short-term deterioration could be seen.

1991; Nygren, 2011). The measurement is not photon statistics-limited, as similar asymptotic values were obtained for different optical gains (up to a number of detected photoelectrons per electron $n_{pe} = 10$). Further, similar results were obtained both with a double-mesh and with a drift-less configuration (the latter being more immune to attachment). The deviation from the Fano limit can be qualitatively understood from the afterpulsing of this PMT model (as observed during the LED characterization): it appears with a delay of about 250 ns, and can reach about 10% of the signal; as the ionization cloud spreads over at least a few µs due to the combined effects of the photoelectron range and diffusion, afterpulsing can not be removed and its event-by-event fluctuations are not correctable.

Notwithstanding, an extrapolation of present results up to the $Q_{\beta\beta}$-scale of ^{136}Xe (2.45 MeV) indicates that the achieved energy resolution is competitive with the ones reached by current experiments and other R&D efforts (Figure 13). The recent result of 0.73% at 1.836 MeV (star), reported for Teflon-based perforated structures in (Akiyama, 2023), gives further support to the notion that, in practical applications, this type of EL-structures are already within the double-mesh performance limit in terms of optical gain and energy resolution.

FIGURE 13
Energy resolution in this work (dark-blue circle) and comparison with other experiments (Figure adapted from (Saa Hernández et al., 2021), with data from (Bolozdynya et al., 1997; Lorca et al., 2014; Ban et al., 2017; Martínez-Lema et al., 2018; Renner et al., 2019; The NEXT collaboration et al., 2019; Akiyama, 2023)). The Fano factor represented by the dashed line is an average value from (De Lima et al., 1982; Henriques, 2018; Anderson et al., 1979; Biagi, 2024; Dias et al., 1991; Nygren, 2011), while the band shows the region comprising the highest and lowest values, considering the entire energy range involved.

To better understand the present technology limits, it is relevant to estimate the wavelength-shifting-efficiency (WLSE) achieved for the TPB-coating process inside the structure channels. The ratio of the TPB-coated structure to the non-coated one has been used for this purpose, as the ratio should be more immune to mis-modeling effects (Figure 14). The uncertainty band was taken to be 15%. As shown, the estimated WLSE of the TPB lies within the 74%–128% range, centered at 105%, in line with the literature results (Kuźniak and Szelc, 2020; Araujo et al., 2022). Simulations performed for the structure with ESR produced slightly lower values of the WLSE of around 94%, that could point to a bad optical coupling (or modeling) of the ESR reflector.
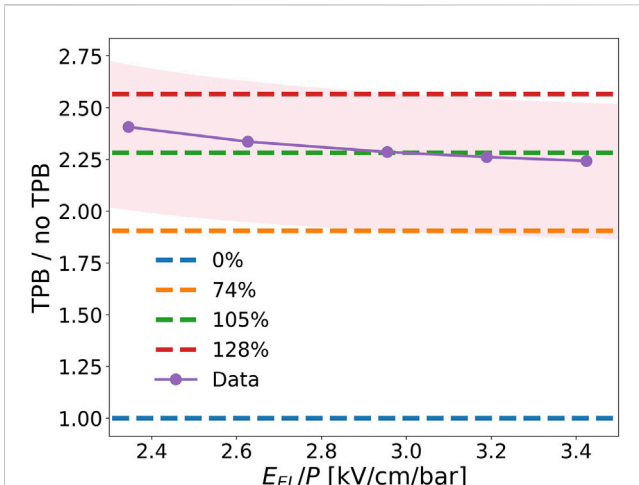
FIGURE 14
Ratio of the light yield of the TPB-coated FAT-GEM to the uncoated one (purple circles), as a function of the pressure-reduced electric field, obtained in xenon at 4 bar. The light-red band accounts for the systematic uncertainty in data. Wavelength-shifting-efficiency (WLSE) has been estimated by comparison with the ratio predicted in simulations (WLSE values indicated by dashed lines).
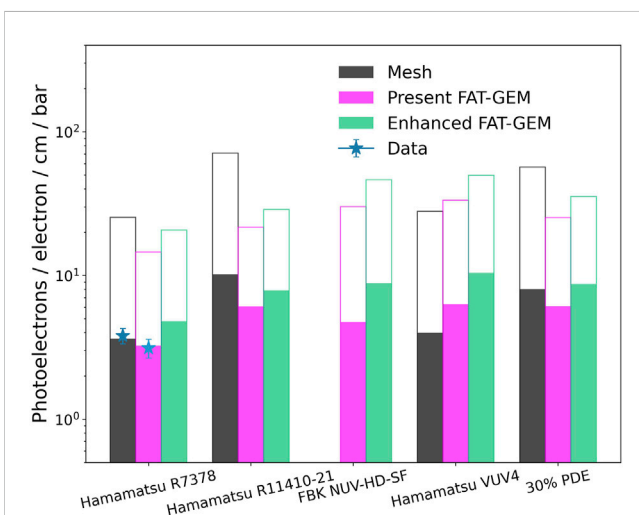

FIGURE 15
Simulated light yields in phe/e/cm/bar when considering the PDE's of different photosensors, for a pressure-reduced field of 3.65 kV/cm/bar, p = 4 bar and a gas gap of 5 mm. The empty bars refer to a half-hemisphere sensor, while the full bars assume the geometry in this work (2.1 cm diameter photosensor at 1.5 cm distance). The structures considered are a double-mesh (black), the FAT-GEM developed in this work (pink), and an "enhanced" FAT-GEM after the modifications discussed in text (green). The blue stars refer to experimental data in this work.

The process of wavelength-shifting results in a different spectral content for the FAT-GEM and double-mesh configurations, so it is interesting to perform a comparison for different photosensors, based on the results achieved in this work. Figure 15 shows the simulated number of photoelectrons (normalized to cm·bar) assuming the nominal PDE of each of the four exemplary photosensors discussed here (meshes in black, FAT-GEM (present) in pink, FAT-GEM (enhanced) in green).

Moreover, a flat-response light sensor with 30% PDE is also shown. The 'enhanced' version of the FAT-GEM assumes a diffuse reflector instead of ESR to minimize the effect of photon trapping due to internal reflection inside the PMMA. Experimental data obtained in this work are given by stars (p = 4 bar). All comparisons have been made at a pressure-reduced electric field of E_{EL} = 3.65 kV/cm/bar for which discharge-free operation of the FAT-GEM was comfortably achieved. Extrapolations to a half-hemisphere photosensor plane are shown by the empty bar.

7 Conclusion

The use of 'ad hoc' perforated structures for electroluminescence is reaching maturity. Here we present performances for the FAT-GEM technology (Field-Assisted Transparent Gaseous Electroluminescence Multipliers), that are already matching those achievable for double-meshes, our proxy for the 'ideal' uniform-field situation. The optical gain achieved in xenon at 4 bar, at a pressure-reduced electric field of 3.65 kV/cm/bar, is within 18% of the value achieved in a double-mesh configuration with the same photosensor coverage, a bit over the systematic uncertainty of present data (15%). Further, a good description of the observed yields can be achieved if assuming a WLSE of 105% for the TPB-coated channels. The structure is electrically stable at 3.65 kV/cm/bar (4 bar) and 2.8 kV/cm/bar (10 bar), the latter limited by the maximum power supply of our equipment. Despite being in a high-field region, no systematic TPB degradation was observed during 20 h of continuous operation. Assuming complete hemispherical coverage, the above WLSE figure extrapolates to a number of detected photoelectrons (at 4 bar) in the range of: 29 (41) for Hamamatsu R7378 PM, 43 (57) for Hamamatsu R11410-21 PM, 60 (92) for FBK NUV-HD-SF SiPM and 66 (99) for Hamamatsu VUV4 SiPM when considering the present (or enhanced) FAT-GEM structures. Higher values are anticipated at higher pressures. The observed energy resolution, on the other hand, extrapolates to 0.84% (0.91%) FWHM for 4 bar (10 bar) at the $Q_{\beta\beta}$ of ^{136}Xe, competitive for next-generation $\beta\beta0\nu$ experiments. Evidence has been presented, pointing to the intrinsic resolution of the structure being better than that.

The FAT-GEM concept combines the properties of gas scintillation and light-guides, being radiopure, versatile in design and intrinsically transparent from the hard VUV up to visible and near-IR regions (1,600 nm). It is called to solve the scaling issues for large-volume chambers and perhaps offer an universal technique to implement electroluminescence readouts in noble-elements.

Data availability statement

The raw data supporting the conclusion of this article will be made available by the authors, without undue reservation.

Author contributions

SL: Data curation, Formal analysis, investigation, software, visualization, Writing–review and editing, Writing–original draft. AS-H: Software, Writing–review and editing. MK: Conceptualization, funding acquisition, Resources, Software,

Conflict of interest

The authors declare that the research was conducted in the absence of any commercial or financial relationships that could be construed as a potential conflict of interest.

The author(s) declared that they were an editorial board member of Frontiers, at the time of submission. This had no impact on the peer review process and the final decision.

Publisher's note

All claims expressed in this article are solely those of the authors and do not necessarily represent those of their affiliated organizations, or those of the publisher, the editors and the reviewers. Any product that may be evaluated in this article, or claim that may be made by its manufacturer, is not guaranteed or endorsed by the publisher.

References

Aalbers, J., Akerib, D. S., Akerlof, C. W., Al Musalhi, A. K., Alder, F., Alqahtani, A., et al. (2023). LUX-ZEPLIN collaboration. *Phys. Rev. Lett.* 131, 041002.

Aalseth, C. E., Abdelhakim, S., Acerbi, F., Agnes, P., Ajaj, R., Albuquerque, I., et al. (2020). Design and construction of a new detector to measure ultra-low radioactive-isotope contamination of argon. *JINST* 15, P02024. doi:10.1088/1748-0221/15/02/p02024

Aalseth, C. E., Acerbi, F., Agnes, P., Albuquerque, I. F. M., Alexander, T., Alici, A., et al. (2018). DarkSide-20k: a 20 tonne two-phase LAr TPC for direct dark matter detection at LNGS. *Eur. Phys. J. Plus* 133, 131. doi:10.1140/epjp/i2018-11973-4

Agnes, P., Albuquerque, I. F. M., Alexander, T., Alton, A. K., Ave, M., Back, H. O., et al. (2023). Search for low-mass dark matter WIMPs with 12 ton-day exposure of DarkSide-50. *Phys. Rev. D.* 107, 063001. doi:10.1103/physrevd.107.063001

Agostinelli, S., Allison, J., Amako, K., Apostolakis, J., Araujo, H., Arce, P., et al. (2003). Geant4—a simulation toolkit. *Nucl. Instrum. Methods Phys. Res. Sect. A Accel. Spectrom. Detect. Assoc. Equip.* 506 (3), 250–303. doi:10.1016/s0168-9002(03)01368-8

Akimov, D.Yu., Alexandrov, I., Alyev, R., Belov, V., Bolozdynya, A., Etenko, A., et al. (2022). The RED-100 experiment. *JINST* 17, T11011. doi:10.1088/1748-0221/17/11/t11011

Akiyama, S. (2023). Status and prospects of the AXEL experiment, *talk at workshop on xenon detector 0νββ searches 2023, SLAC.*

Alves, M. A. F., and Policarpio, A. (1967). The effect of a wave-length shifter on the light output of the ArN2 proportional scintillation counter. *Nucl. Instrum. Methods* 57, 321–324. doi:10.1016/0029-554x(67)90542-3

Amaudruz, P.-A., Baldwin, M., Batygov, M., Beltran, B., Bina, C. E., Bishop, D., et al. (2019). Design and construction of the DEAP-3600 dark matter detector. *Astropart. Phys.* 108, 1–23. doi:10.1016/j.astropartphys.2018.09.006

Anderson, D. F., Hamilton, T., Ku, W. M., and Novick, R. (1979). A large area, gas scintillation proportional counter. *Nucl. Instrum. Methods* 163, 125–134. doi:10.1016/0029-554x(79)90040-5

ANSYS (2023). Available online: https://www.ansys.com/products (visited on September 19, 2023).

Application Guidelines ESR Family. 2018. Application Guidelines ESR family. Available online: https://multimedia.3m.com/mws/media/1389248O/application-guide-for-esr.pdf (accessed on 1 November 2023).

Aprile, E., Abe, K., Agostini, F., Ahmed Maouloud, S., Althueser, L., Andrieu, B., et al. (2023). First dark matter search with nuclear recoils from the XENONnT experiment. *Phys. Rev. Lett.* 131, 041003. doi:10.1103/PhysRevLett.131.041003

Aprile, E., Bolotnikov, A. E., Bolozdynya, A. I., and Doke, T. (2006). *Noble gas detectors.* Wiley VCH.

Araujo, G. R., Baudis, L., McFadden, N., Krause, P., Schönert, S., and Wu, V. H. S. (2022). R &D of wavelength-shifting reflectors and characterization of the quantum efficiency of tetraphenyl butadiene and polyethylene naphthalate in liquid argon. *Eur. Phys. J. C* 82, 442. doi:10.1140/epjc/s10052-022-10383-0

Azevedo, C. D. R., Gonzalez Diaz, D., Biagi, S., Oliveira, C. A. B., Henriques, C., Escada, J., et al. (2018). Microscopic simulation of xenon-based optical TPCs in the presence of molecular additives. *Nucl. Instrum. Methods Phys. Res. Sect. A Accel. Spectrom. Detect. Assoc. Equip.* 877, 157–172. doi:10.1016/j.nima.2017.08.049

Azevedo, C. D. R., Pereira, F., Lopes, T., Correia, P., Silva, A., Carramate, L., et al. (2013). A gaseous Compton camera using a 2D-sensitive gaseous photomultiplier for nuclear medical imaging. *Nucl. Instrum. Methods Phys. Res. Sect. A Accel. Spectrom. Detect. Assoc. Equip.* 732, 551–555. doi:10.1016/j.nima.2013.05.116

Ban, S., Nakamura, K. D., Hirose, M., Ichikawa, A. K., Minamino, A., Miuchi, K., et al. (2017). Electroluminescence collection cell as a readout for a high energy resolution Xenon gas TPC. *Nucl. Instrum. Methods Phys. Res. Sect. A Accel. Spectrom. Detect. Assoc. Equip.* 875, 185–192. doi:10.1016/j.nima.2017.09.015

Benson, C., Orebi Gann, G. D., and Gehman, V. (2018). Measurements of the intrinsic quantum efficiency and absorption length of tetraphenyl butadiene thin films in the vacuum ultraviolet regime. *Eur. Phys. J. C* 78, 329. doi:10.1140/epjc/s10052-018-5807-z

Biagi, S. (2024). Degrad - transport of electrons in gas mixtures. Available online: https://degrad.web.cern.ch/degrad/ (visited on January 09, 2024).

Blum, W., Riegler, W., and Rolandi, L. (2008). *Particle detection with drift chambers*. Springer Verlag.

Bolozdynya, A., Egorov, V., Koutchenkov, A., Safronov, G., Smirnov, G., Medved, S., et al. (1997). A high pressure xenon self-triggered scintillation drift chamber with 3D sensitivity in the range of 20–140 keV deposited energy. *Nucl. Instrum. Methods Phys. Res. Sect. A Accel. Spectrom. Detect. Assoc. Equip.* 385, 225–238. doi:10.1016/s0168-9002(96)01035-2

Bondar, A., Buzulutskov, A., Frolov, E., Borisova, E., Nosov, V., Oleynikov, V., et al. (2023). First observation of neutral bremsstrahlung electroluminescence in liquid argon. *Phys. Rev. Lett.* 131, 241001. doi:10.1103/physrevlett.131.241001

Boulay, M. G., Camillo, V., Canci, N., Choudhary, S., Consiglio, L., Flammini, A., et al. (2021). Direct comparison of PEN and TPB wavelength shifters in a liquid argon detector. *Eur. Phys. J. C* 81, 1099. doi:10.1140/epjc/s10052-021-09870-7

Conde, C. A. N., and Policarpo, A. J. P. L. (1967). A gas proportional scintillation counter. *Nucl. Instrum. Methods* 53, 7–12. doi:10.1016/0029-554x(67)91323-7

Conde, C. A. N., Policarpo, A. J. P. L., and Alves, M. A. F. (1968). Gas proportional scintillation counter with xenon and xenon mixtures. *IEEE Trans. Nucl. Sci.* 15 (3), 84–91. doi:10.1109/tns.1968.4324919

De Lima, E. P., Salete, M., Leite, S. C. P., Alves, M. A. F., and Policarpo, A. J. P. L. (1982). Fano factors of rare gases and their mixtures. *Nucl. Instrum. Methods Phys. Res.* 192 (2–3), 575–581.

Dias, T. H. V. T., Santos, F., Stauffer, A., and Conde, C. (1991). The Fano factor in gaseous xenon: a Monte Carlo calculation for X-rays in the 0.1 to 25 keV energy range. *Nucl. Instrum. Methods Phys. Res. Sect. A Accel. Spectrom. Detect. Assoc. Equip.* 307, 341–346. doi:10.1016/0168-9002(91)90202-2

Discussions at the Conference (2023). *Light detection in noble elements*. (LIDINE), Madrid. doi:10.48550/arXiv.2305.09435

Escada, J., Dias, THVT, Santos, F. P., Rachinhas, PJBM, Conde, C. A. N., and Stauffer, A. D. (2011). A Monte Carlo study of the fluctuations in Xe electroluminescence yield: pure Xe vs Xe doped with CH_4 or CF_4 and planar vs cylindrical geometries. *J. Instrum.* 6, P08006. doi:10.1088/1748-0221/6/08/p08006

Freitas, E. D. C., Monteiro, C. M. B., Ball, M., Gómez-Cadenas, J. J., Lopes, J. A. M., Lux, T., et al. (2010). Secondary scintillation yield in high-pressure xenon gas for neutrinoless double beta decay (0νββ) search. *Phys. Lett. B* 684, 205–210. doi:10.1016/j.physletb.2010.01.013

Gallina, G., Giampa, P., Retière, F., Kroeger, J., Zhang, G., Ward, M., et al. (2019). Characterization of the hamamatsu VUV4 MPPCs for nEXO. *Nucl. Instrum. Methods Phys. Res. Sect. A Accel. Spectrom. Detect. Assoc. Equip.* 940, 371–379. doi:10.1016/j.nima.2019.05.096

González-Díaz, D., Fontaíña, M., García Castro, D., Mehl, B., De Oliveira, R., Williams, S., et al. (2020). A new amplification structure for time projection chambers based on electroluminescence. *J. Phys. Conf. Ser.* 1498, 012019. doi:10.1088/1742-6596/1498/1/012019

hamamatsu.com (2024). hamamatsu.com. Available online: https://www.datasheet.live/pdfviewer?url=https%3A%2F%2Fpdf.datasheet.live%2F6432b002%2Fhamamatsu.com%2FR7378.pdf (visited on January 09, 2024).

Henriques, C. (2018). "Studies of xenon mixtures with molecular additives for the NEXT electroluminescence TPC,". PhD thesis.

Henriques, C. A. O., Amedo, P., Teixeira, J. M. R., González-Díaz, D., Azevedo, C. D. R., Para, A., et al. (2022). Neutral bremsstrahlung emission in xenon unveiled. *Phys. Rev. X* 12, 021005. doi:10.1103/physrevx.12.021005

Henriques, C. A. O., Freitas, E. D. C., Azevedo, C. D. R., González-Díaz, D., Mano, R. D. P., Jorge, M. R., et al. (2017). Secondary scintillation yield of xenon with sub-percent levels of CO2 additive for rare-event detection. *Phys. Lett. B* 773, 663–671. doi:10.1016/j.physletb.2017.09.017

Irastorza, I. G., Ferrer-Ribas, E., and Dafni, T. (2013). Micromegas in the rare event searches field. *Mod. Phys. Lett. A* 28, 1340026. doi:10.1142/s0217732313400269

Kuźniak, M., González-Díaz, D., Amedo, P., Azevedo, C., Fernández-Posada, D., Kuźwa, M., et al. (2021). Development of very-thick transparent GEMs with wavelength-shifting capability for noble element TPCs. *Eur. Phys. J. C* 81, 609. doi:10.1140/epjc/s10052-021-09316-0

Kuźniak, M., and Szelc, A. M. (2020). Wavelength shifters for applications in liquid argon detectors. *Instruments* 5, 4. doi:10.3390/instruments5010004

Leardini, S., García, E. S., Amedo, P., Saa-Hernández, A., González-Díaz, D., Santorelli, R., et al. (2022). Time and band-resolved scintillation in time projection chambers based on gaseous xenon. *Eur. Phys. J. C* 82, 425. doi:10.1140/epjc/s10052-022-10385-y

Lindseth, I., Bardal, A., and Spooren, R. (1999). Reflectance measurements of aluminium surfaces using integrating spheres. *Opt. Lasers Eng.* 32 (5), 419–435. doi:10.1016/s0143-8166(00)00010-5

Lorca, D., Martín-Albo, J., Laing, A., Ferrario, P., Gómez-Cadenas, J. J., Alvarez, V., et al. (2014). Characterisation of NEXT-DEMO using xenon K_α X-rays. *J. Instrum.* 9, P10007. doi:10.1088/1748-0221/9/10/P10007

Lowe, A., Majumdar, K., Mavrokoridis, K., Philippou, B., Roberts, A., and Touramanis, C. (2021). A novel manufacturing process for glass THGEMs and first characterisation in an optical gaseous argon TPC. *Appl. Sci.* 11, 9450. doi:10.3390/app11209450

Lowe, A. J., Amedo-Martinez, P., González-Díaz, D., Deisting, A., Majumdar, K., Mavrokoridis, K., et al. (2023). ARIADNE+: large scale demonstration of fast optical readout for dual-phase LArTPCs at the CERN neutrino platform. *NuFACT 2022* 8, 46. doi:10.3390/psf2023008046

Martínez-Lema, G., Morata, J. H., Palmeiro, B., Botas, A., Ferrario, P., Monrabal, F., et al. (2018). Calibration of the NEXT-White detector using 83mKr decays. *JINST* 13, P10014. doi:10.1088/1748-0221/13/10/p10014

Monrabal, F. (2021). Gaseous detectors for Neutrino-nucleus coherent scattering at the ESS. *J. Phys. Conf. Ser.* 2156, 012112. doi:10.1088/1742-6596/2156/1/012112

Monteiro, C., Fernandes, L., Veloso, J., Oliveira, C. A. B., and dos Santos, J. (2012). Secondary scintillation yield from GEM and THGEM gaseous electron multipliers for direct dark matter search. *Phys. Lett. B* 714, 18–23. doi:10.1016/j.physletb.2012.06.066

Monteiro, C. M. B., Lopes, J., Veloso, J., and dos Santos, J. (2008). Secondary scintillation yield in pure argon. *Phys. Lett. B* 668, 167–170. doi:10.1016/j.physletb.2008.08.030

Müller, J. The PANCAKE detector development platform for multi-ton LXe detectors 2022, talk at XeSAT, Coimbra.

Norman, L., Silva, K., Jones, B. J. P., McDonald, A. D., Tiscareno, M. R., and Woodruff, K. (2022). Dielectric strength of noble and quenched gases for high pressure time projection chambers. *Eur. Phys. J. C* 82, 52. doi:10.1140/epjc/s10052-021-09894-z

Novella, P., Sorel, M., Usón, A., Adams, C., Almazán, H., Álvarez, V., et al. (2023). Demonstration of neutrinoless double beta decay searches in gaseous xenon with NEXT. *J. High. Energ. Phys.* 2023, 190. doi:10.1007/jhep09(2023)190

Novella, P., Sorel, M., Usón, A., Adams, C., Almazán, H., álvarez, V., et al. (2022). Measurement of the ${}^{136}\mathrm{Xe}$ two-neutrino double-$\ensuremath{\beta}$-decay half-life via direct background subtraction in NEXT. *Phys. Rev. C* 105 (5), 055501. doi:10.1103/physrevc.105.055501

Nygren, D. (2009). High-pressure xenon gas electroluminescent TPC for 0-ν ββ-decay search. *Nucl. Instrum. Methods Phys. Res. Sect. A Accel. Spectrom. Detect. Assoc. Equip.* 603, 337–348. doi:10.1016/j.nima.2009.01.222

Nygren, D. (2011). *J. Phys. Conf. Ser.* 309, 012006. doi:10.1088/1742-6596/309/1/012006

Oliveira, C. A. B., Schindler, H., Veenhof, R., Biagi, S., Monteiro, C., dos Santos, J., et al. (2011). A simulation toolkit for electroluminescence assessment in rare event experiments. *Phys. Lett. B* 703, 217–222. doi:10.1016/j.physletb.2011.07.081

PandaX Collaboration (2023). Limits on the luminance of dark matter from xenon recoil data. *Nature* 618, 47–50. doi:10.1038/s41586-023-05982-0

PhotoMultiplier tubes and assemblies (2024). PhotoMultiplier tubes and assemblies for scintillation counting & high energy physics. Available online: https://www.hamamatsu.com/content/dam/hamamatsu-photonics/sites/documents/99_SALES_LIBRARY/etd/High_energy_PMT_TPMZ0003E.pdf (visited on January 10, 2024).

Renner, J., Díaz López, G., Ferrario, P., Hernando Morata, J. A., Kekic, M., Martínez-Lema, G., et al. (2019). Energy calibration of the NEXT-White detector with 1% resolution near $Q_{\beta\beta}$ of ^{136}Xe. *J. High. Energ. Phys.* 2019, 230. doi:10.1007/jhep10(2019)230

Rogers, L., Clark, R., Jones, B., McDonald, A., Nygren, D., Psihas, F., et al. (2018). High voltage insulation and gas absorption of polymers in high pressure argon and xenon gases. *JINST* 13, P10002. doi:10.1088/1748-0221/13/10/p10002

Saa Hernández, A., González-Díaz, D., and Azevedo, C. D. R. (2021). *Radiation detection systems*. 2nd Edition, chapter 10. Boca Raton: CRC Press. Xenon-Based EL-TPCs for 4π Detection of X-Rays in the Energy Range 10–100 keV.

Saá-Hernández, A., González-Díaz, D., Villanueva, P., Azevedo, C., and Seoane, M. (2021). A new imaging technology based on Compton X-ray scattering. *J. Synchrotron Radiat.* 28, 1558–1572. doi:10.1107/s1600577521005919

Schindler, H. (2019). Garfield++. Available online: https://garfieldpp.web.cern.ch/garfieldpp/ (visited on September 19, 2023).

Serra, L., Sorel, M., Álvarez, V., Borges, F. I. G., Camargo, M., Cárcel, S., et al. (2015). An improved measurement of electron-ion recombination in high-pressure xenon gas. *JINST* 10, P03025. doi:10.1088/1748-0221/10/03/p03025

Takahashi, H., Mitsuya, Y., Fujiwara, T., and Fushie, T. (2013). Development of a glass GEM. *Nucl. Instrum. Methods Phys. Res. Sect. A Accel. Spectrom. Detect. Assoc. Equip.* 724, 1–4. doi:10.1016/j.nima.2013.04.089

Tameda, Y., Tomida, T., Yamamoto, M., Iwakura, H., Ikeda, D., and Yamazaki, K. (2019). Air shower observation by a simple structured Fresnel lens telescope with a single pixel for the next generation of ultra-high-energy cosmic ray observatories. *Prog. Theor. Exp. Phys.* 2019 (4), 043F01. doi:10.1093/ptep/ptz025

The, NEXT collaborationHenriques, C. A. O., Monteiro, C. M. B., González-Díaz, D., et al. (2019). Electroluminescence TPCs at the thermal diffusion limit. *J. High. Energ. Phys.* 27.

Visiontek Systems Ltd. (2023). Visiontek systems. Available online: https://www.visionteksystems.co.uk/ito_conductive_film.htm (Accessed October 15, 2023).

Weber, M. F., Stover, C. A., Gilbert, L. R., Nevitt, T. J., and Ouderkirk, A. J. (2000). Giant birefringent optics in multilayer polymer mirrors. *Science* 287, 2451–2456. doi:10.1126/science.287.5462.2451